HHS Public Access

Author manuscript

Physiol Meas. Author manuscript; available in PMC 2018 June 08.

Published in final edited form as:

Physiol Meas. 2017 March ; 38(3): 452–465. doi:10.1088/1361-6579/aa577b.

Customized compact neutron activation analysis system to quantify manganese (Mn) in bone *in vivo*

Yingzi Liu, **Farshad Mostafaei**, **Daniel Sowers**, **Mindy Hsieh**, **Wei Zheng**, and **Linda H Nie**[1]

School of Health Sciences, Purdue University, West Lafayette, United States of America

Abstract

Objective—In the US alone, millions of workers, including over 300 000 welders, are at high risk of occupational manganese (Mn) exposure. Those who have been chronically exposed to excessive amount of Mn can develop severe neurological disorders similar, but not identical, to the idiopathic Parkinson's disease. One challenge of identifing the health effects of Mn exposure is to find a reliable biomarker for exposure assessment, especially for long-term cumulative exposure.

Approach—Mn's long biological half-life as well as its relatively high concentration in bone makes bone Mn (BnMn) a potentially valuable biomarker for Mn exposure. Our group has been working on the development of a deuterium–deuterium (D–D)-based neutron generator to quantify Mn in bone *in vivo*.

Main results and significance—In this paper, we report the latest advancements in our system. With a customized hand irradiation assembly, a fully characterized high purity germanium (HPGe) detector system, and an acceptable hand dose of 36 mSv, a detection limit of 0.64 μg Mn/g bone (ppm) has been achieved.

Keywords

neutron activation analysis; manganese; MCNP

1. Introduction

Over the last decades, growing public concern on the detrimental health effects of Mn overexposure has been raised. Mn is the fourth most utilized metal in modern industries, notably in steel manufacturing and welding (Wang *et al* 1989, Bouaziz *et al* 2011). Workers in those industries are at high risk of elevated Mn exposure, including Mn miners who are continuously engaged in Mn production and processing. In addition, the general population can be exposed to this toxic metal by environmental routes, such as Mn-containing pesticides, contaminated water and food (Bouchard *et al* 2011), and organic Mn compounds in gasoline (Butcher *et al* 1999). Moreover, there have been reports on excessive Mn intake among ephedron drug abusers (Yildirim *et al* 2009), as well as in patients who are injected with Mn-based contrast probes for magnetic resonance imaging (MRI) screening (Zhen and Xie 2012). Claims of Mn poisoning have been raised worldwide since 1837, describing various neurological disorders; in severe cases, a devastating neurological impairment

[1]Author to whom any correspondence should be addressed. hnie@purdue.edu.

named ‘manganism’ occurs, with symptoms similar but not identical to the idiopathic Parkinson’s disease (Rodier 1955, Wennberg *et al* 1991, Levy and Nassetta 2003, Crossgrove and Zheng 2004).

Mn-caused neurological damage in patients diagnosed with manganism is usually irreversible, reflecting a permanent structural and functional injury (Huang *et al* 1989, Jiang *et al* 2006, Aschner *et al* 2007). Thus, to prevent the disease, it is imperative to develop an effective means for early assessment of the Mn level stored in the body and for early diagnosis of Mn intoxication. At present, however, there is no reliable biomarker or indicator for Mn exposure. Blood, urine, nail and hair samples have been tested in the past for this purpose, but results were controversial and, in many cases, they were not associated with the Mn exposure levels. Mn levels in nail and hair samples are promising, yet they are readily subjected to external contaminations. More recently, the MRI technology can detect and quantify Mn concentrations in specific regions of the brain (Crossgrove and Zheng 2004). However, several months after removal from the Mn sources, the Mn signal can disappear while the neurological dysfunctions remain. Thus, a novel approach to assess chronic deposition of Mn in the body is highly desirable.

Bones have been proposed as a potential reliable biomarker for two reasons. First, Mn in bones has a long biological half-life, and second, bones serve as the primary storage organ for Mn in the body (Arnold *et al* 2002). Currently, there are no data reflecting the retention rate of Mn in human bone. In animal models, our recent study on a rat model suggests that the average half-life of Mn in rat bone is approximately 143 d for chronical oral exposure, which is equivalent to 8.5 years in human bone (O’Neal *et al* 2014). The data indicate that bone has a much longer half-life than other tissues. The concentration of Mn in bone can be derived from data given in International Commission on Radiological Protection (ICRP) 23 and ICRP 70 (Snyder *et al* 1975, Valentin 2002). The estimated value was 1 μg Mn per g bone, which is equivalent to 5 μg Mn per g Ca. The World Health Organization (WHO) reports that the Reference Man contains about 12 000 μg Mn in the entire body, with the range from 10 000 to 20 000 μg (World Health Organization 1981). Given that 5423 μg Mn is in bone (ICRP 23), it is reasonable to suggest that between 27.1% and 54.2% of body Mn is stored in bone with an average of 45.2%. Based on the aforementioned estimates, it is logical to predict that in humans, bone is the primary organ for long-term Mn storage, and thus, MnBn may provide information on neurological functions if such a relationship can be established among the Mn-exposed workers.

Neutron activation analysis (NAA), which has a long history of use for elemental analysis, can be a powerful modality for *in vivo* MnBn measurement. It uses a low energy (thermal) neutron source to stimulate the production of characteristic gamma rays from a sample. The resulting gamma rays are detected and analyzed to identify and quantify the elements within the sample. While it is desirable to use a nuclear reactor that produces high fluence of thermal neutrons, reactors have disadvantages such as price and safety that limit their application in *in vivo* NAA. Currently the only operating system available for bone Mn assessment is located at McMaster University in Canada (Pejovic-Milic *et al* 2008a, 2009). The system, however, is a laboratory accelerator-based NAA system and requires a Tandetron accelerator, a large laboratory space of over 800 square feet, and a trained

operator to monitor the process. For these reasons, this system is not practical for on-site human field studies. Recently, the development of a compact deuterium–deuterium (D–D) neutron generator offers distinct advantages over other systems because of its smaller size, lower price, easier mobility and better security. Therefore, D–D neutron generator has become our choice as the neutron source for NAA.

In this paper, we report the latest development of a compact D–D NAA system: a customized irradiation assembly that maximizes the thermal neutron flux, a fully characterized high purity germanium (HPGE) detector system with an established absolute efficiency, and an improved detection limit based on the phantom study. The neutron and photon irradiation doses were also estimated through simulations and measurements. This work clearly illustrates the capability of the D–D NAA system for *in vivo* quantification of Mn in human bone, suggesting a path toward understanding of Mn overexposure using bone Mn as the biomarker.

2. Material and methods

Samples are first activated in the irradiation assembly, then transferred to the measurement site to capture the emission of ^{56}Mn. The detection limit can then be determined based on the sample signals. The subsequent sections in Material and methods are outlined as the following: the *in vivo* neutron activation analysis technology (section 2.1); the type of neutron source used in this study (section 2.2); the Monte Carlo (MC) program used for system design and characterization (section 2.3); detection system (section 2.4); sample preparation (section 2.5); detection limit (section 2.6); methods to measure the irradiation dose (section 2.7).

2.1. In vivo neutron activation analysis

In vivo NAA is a promising diagnostic technique that allows noninvasive quantification of various elements in the human body. Mn NAA is based on the neutron activation reaction of natural Mn, ^{55}Mn(n, γ) ^{56}Mn, and detection of the resulting 847 keV characteristic gamma rays from the decay of ^{56}Mn ($T_{1/2}$ = 2.58 h). Quantification of the 847 keV gamma rays in counts (C) is determined by:

$$C = \frac{N_{\mathrm{av}}\theta m}{M\lambda}(1-\mathrm{e}^{-\lambda t_{\mathrm{i}}})\mathrm{e}^{-\lambda t_{\mathrm{d}}}(1-\mathrm{e}^{-\lambda t_{\mathrm{m}}})\varepsilon\Gamma\int_{E_{\mathrm{min}}}^{E_{\mathrm{max}}}\phi(E)\sigma(E)\mathrm{d}E$$

where t_{i} is the sample irradiation time; t_{d} is the decay time; t_{m} is the measurement time; N_{av} is the Avogadro's number; θ is the isotopic abundance of the target isotope; m is the mass of the irradiated element; M is the atomic mass; Γ is the gamma-ray abundance; ε is the absolute photon-peak efficiency of the detector; $\phi(E)$ is the neutron fluence with respect to energy and $\sigma(E)$ is the corresponding cross section.

The irradiation factor ($1 - \mathrm{e}^{-\lambda t_{\mathrm{i}}}$) needs to be as high as possible but is limited by the maximum permissible radiation dose to the tissue (no larger than 50 mSv). Ten min was decided to be the irradiation time based on the compromise between the two.

Decay time ($e^{-\lambda t_d}$) needs to be as short as possible. However, because the decay time of ^{56}Mn is 2.58 h, the signal does not change much when the decay time is 10 min instead of 1 min. 10 min will give us enough time to take the sample out from the irradiation site, transport it to the measurement site and take the measurement.

Measurement time needs to be as long as possible ($1 - e^{-\lambda t_m}$), but since this is a human study, some practical issue was taken into account and 30 min was determined to be acceptable.

$\sigma(E)$ is inversely correlated to the incident neutron energy. Therefore, in order to maximize the system's detection limit of 847 keV gamma counts in a Mn sample, the incident neutron energy should be decelerated to as low as possible. The system's detection limit can be further improved by improving the detector's absolute efficiency ε and increasing the thermal neutron flux $\phi(E)$.

2.2. Deuterium–deuterium neutron generator

A D–D neutron generator (DD-109; Adelphi Technology Inc., Redwood, CA) was used in this study. It produces mono-energetic 2.45 MeV neutrons (${}^{2}_{1}\mathrm{D} + {}^{2}_{1}\mathrm{D} \rightarrow {}^{3}_{2}\mathrm{He} + n$) in an approximately isotropic manner. The deuterium gas is first ionized by a magnetron and then accelerated to a titanium target. The titanium target becomes saturated with deuterium over the first several seconds of operation, which then results in a steady-state production of neutrons. Throughout the experiments, the generator was operated at the following setting: accelerator voltage at 120 kV, magnetron voltage and current at 80 kV and 5 mA, and deuterium gas pressure flow at 1.2 standard cubic centimeters per minute (SCCM), or 5 mTorr. Under these parameters, the D–D neutron generator emits approximately 7×10^8 neutrons per second (Liu *et al* 2014).

In addition to neutrons, high intensity x-rays are produced simultaneously when operating the D–D neutron generator. When the titanium target is bombarded with deuterons, electrons are produced and accelerated in the opposite direction, striking the aluminum plate at the ion source aperture and producing a spectrum of bremsstrahlung x-rays. These x-rays have an average energy of 40 keV and a maximum of 120 keV.

2.3. Monte Carlo simulation

In radiation physics, Monte Carlo (MC) computer simulation has been widely applied for solving the Boltzmann transportation equation. In this work, MC calculations were performed with MCNPX 2.7.0, a multipurpose code that provides an almost complete description of particle transport for neutrons, photons, and electrons. Figure 1 illustrates a 2D schematic plot and a MCNPX 3D view of the neutron generator model. Moderating, reflecting and shielding materials were subsequently added to compute the spectra and radiation doses. Since complicated geometries and mesh tallies often take a great deal of computational time, the input files were submitted to Purdue's high performance computer cluster, Hansen, which is comprised of four-socket 12-core AMD Opteron 6176 CPUs and 10 Gbit Ethernet. The required particle histories were set to ensure that uncertainties were less than 5%.

2.4. Signal detection and processing

In this study, a high purity germanium (HPGe) detector (GMX90P4-ST; Ortec®, Oak Ridge, TN) was utilized for γ-ray detection. The signals were processed and collected by DSPEC plus and Maestro γ-ray spectroscopy. The absolute efficiency at certain energy is related to the performance of the detector as well as the specific geometry of the sample. Moreover, efficiency calibration curve developed by multi-nuclide standard source needs to be corrected for coincident summing effect because when the source is placed very close to the detector window, summing effect can cause underestimation of the radionuclides' efficiencies. Since it is difficult to analytically calculate these three factors, MC simulations were carried out to model the HPGe detector head with parameters provided by the manufacturer (figure 2). A multi-nuclide standard source (Catalog No. 7500; Eckert & Ziegler Isotope Products, Inc. Valencia, CA) comprising Cd-109, Co-57, Te-123m, Sn-113 and Cs-137 and two standard point sources, Am-241 (59.54 keV) and Cs-137 (662 keV), were used to compare simulation and experimental results. In the simulation, the dead layer thickness and distance of Ge crystal from the Al window were adjusted from the values given by the manufacturer until the differences between simulation and experimental results were within 10%. Once the MCNP model was validated, the detection efficiencies at any given distance and geometry could be precisely calculated by MC simulation.

2.5. Mn doped phantom

The hand was chosen as the measurement site because by stretching the arm into the irradiation assembly, the vital and sensitive organs of the subject's torso can be spared from undesirable irradiations. Five rectangular phantoms were prepared to simulate the hand palm with different concentrations of Mn, 0, 7.5, 15, 22.5, and 30 ppm. Mowiol 4–88 was used as the binding material. Mowiol is a water soluble synthetic polymer with the idealized formula $[CH_2CH(OH)]_n$. It can work as an ideal adhesive to keep the phantom's shape (Mostafaei *et al* 2013b). $Mn(NO_3)_2$ solution was used to provide ^{55}Mn. Chemical compounds containing calcium (Ca), sodium (Na), chlorine (Cl), and magnesium (Mg), which have high neutron capture cross section and are presented in the human bone, were also added. Detailed information about these compounds was described in our previously published paper (Liu *et al* 2014). Since different phantoms were inevitably subjected to the variation of neutron flux, a more appropriate way to estimate the Mn concentration is by applying the Mn/Ca ratio with Ca as an internal standard. The activated Mn and Ca counts are essentially determined by the same thermal neutron flux. Hence, with known concentrations, the Mn/Ca ratio is expected to be the same between experiment and simulation, regardless of the differences in thermal flux.

2.6. Detection limit

The detection limit (DL) of this irradiation system was calculated based on the measurements taken from the Mn-doped phantoms by the following formula:

$$\mathrm{DL} = \frac{2 \times \sqrt{\mathrm{bkg}}}{C}$$

Where the bkg is the background counts under the Mn γ-ray peak for the 0 ppm phantom, and C (counts/ppm) was the slope of the regression line of Mn counts versus Mn concentration (Pejovic-Milic *et al* 2008b, Mostafaei *et al* 2013a). The energy range of the background was estimated as 4 sigma of the Mn γ-ray Gaussian peak, which covers 96% of the peak counts. Sigma was estimated from the fitting program built into the data analysis tool IGOR pro 6 (WaveMetrics, Inc. Lake Oswego, OR, USA).

2.7. Dosimeters

A portable survey meter (NSN3; Fuji Electric Co., Shinagawa-ku, Tokyo, Japan) was used to monitor the neutron dose rate outside the customized blocks. Since it gives the ambient dose equivalent at 1 cm depth based on ICRP 74, the ICRP 74 neutron flux-to-dose conversion factors were employed in the MCNPX simulation to compare and to validate the results with the NSN3 survey meter. An electronic pocket dosimeter (NRF31; Fuji Electric Co., Shinagawa-ku, Tokyo, Japan) and a film badge were also used to measure the neutron dose.

TLD-700 chips (TLD-700™;Thermo Fisher Scientific Inc.) were calibrated with a standard Cs-137 source and placed inside the irradiation cave to measure the photon dose. The over-response of the TLDs was examined by the MCNP simulation and compared to the literature values. For a 40 keV, 65-curie point photon source at 100 cm, MCNP showed that the simulated soft tissue and TLD 700 dose rates were 4.68 and 6.176 mRem h^{-1}, respectively. An over-response of 32% was found with TLD 700, which is consistent with a value of 30%–40% from literature (Chen and McKeever 1997). After validation of the simulation, the Al bremsstrahlung spectrum was modeled as the x-ray source at the neutron generator's ion source aperture to explore the over-response effect under our specific settings. Photon doses at different external spots were measured by a micro-rem gamma survey meter.

3. Results

The results presented in this section loosely follow the order of the methods described in section 2. Section 3.1 shows the final design of the irradiation assembly. Section 3.2 demonstrates the characterization of the detection system. Section 3.3 illustrated the experimental results and the detection limit. Section 3.4 addresses the irradiation doses.

3.1. The design of the irradiation assembly design and flux assessment

Our previously published paper has selected 5 cm of high density polyethylene (HDPE) (with a similar chemical composition and density as paraffin) as the optimal moderator, 10 cm of HDPE as the reflector on the right sid,; and graphite as the reflector on the left side of the generator (Liu *et al* 2013). Those simulations were carried out by choosing the materials that produced the highest thermal neutron yield in the irradiation site. In this work, to further improve the design of the irradiation system, a hand model was simulated in the irradiation site along with a more detailed neutron generator configuration and the neutron flux and spectrum in the hand bone were determined.

The best moderator and reflectors materials were consistent with previously published data but slightly different in the optimal thicknesses (6 cm of HDPE moderator, 8 cm graphite

and 8 cm of HDPE reflector). The thermal neutron enhancement by adding the optimized moderator and reflectors is summarized in figure 3.

Following the simulation results, customized blocks were designed and manufactured to fit the generator head. As shown in figure 4, graphite blocks are represented in yellow, HDPE in green and borated HDPE in red. Additional HDPE blocks were added to further reduce the neutron dose outside the assembly.

3.2. HPGe detector characterization

Large discrepancies in efficiency were observed between experiments and MC simulations when using the manufacturer's parameters. As shown in table 1, before adjustment, nuclides emitting lower energy gammas demonstrated a larger inconsistency. This implies that the actual thickness of the Ge dead layer was larger than the value provided by the manufacturer because gamma attenuation coefficient is inversely proportional to the cubic of gamma energy ($\propto 1/E^3$) when the dominant effect is photoelectric. The simulated Ge dead layer thickness in the MCNP model was increased from 0.7 mm to 1.1 mm to achieve approximately the same inconsistency for all the nuclides. The distance from the Al window to the Ge crystal was then further modified in order to make all the discrepancies within 10%. Table 1 tabulates the experimental and simulated efficiencies for two point sources as well as a multi-nuclide standard source.

Co-60 and Y-88 in the multi-nuclide standard source were not used for detector characterization because of their well-known coincidence summing effect. As shown in figure 5, without correction for the summing effect, there would be a significant underestimation of the efficiency at higher energies. In our situation specifically, underestimation of Y-88 efficiency can be as large as 23% (0.026 04 versus 0.019 96). For energies higher than 1836 keV emitted by Y-88, the discrepancies were even larger.

For our NAA study, the actual efficiencies for Mn and Ca were then determined by simulations with a rectangular phantom placed against the detector's Al window and were found to be 0.048 and 0.021, respectively.

3.3. Hand phantom Mn/Ca ratio and Mn detection limit

Five hand phantoms (Mn concentrations of 0, 7.5, 15, 22.5, 30 ppm) were irradiated in the customized cave for 10 min, followed by 10 min of decay and 30 min of counting. Phantoms were placed closely against the Al window of the HPGe detector. The spectrum obtained from 7.5 ppm hand phantom is displayed in figure 6. The measured Mn, Ca counts and Mn/Ca ratios are listed in table 2. FM4 card in the MCNPX model was used to estimate the activated number of ^{56}Mn. The irradiation, decay, and measurement factors as well as the simulated absolute efficiencies of the HPGe detector for Mn and Ca were added to calculate the simulated Mn/Ca ratios.

The experimental Mn/Ca ratio against Mn concentration calibration line was calculated as $y = 0.0294x + 0.1343$ ($R^2 = 0.968$), while the simulated calibration line was $y = 0.0264x$. The MC simulated slope was in good agreement with the experimental results, which reinforced the usefulness of measuring the Mn/Ca ratio for determination of the Mn concentration in

the samples. The hand phantoms had around 4.6 ppm of Mn contamination. The sources of contaminations might be from the phantom's paper container, the phantom preparation process, and the neutron-induced background signal. The DL was estimated to be 0.64 ppm.

3.4. Flux and irradiation dose

Neutron yield of the neutron generator has been previously studied and calculated as 7×10^8 neutrons/s (Liu *et al* 2014). This paper addresses the flux associated with photons. Without lead shielding, at 100 cm away from the neutron generator head, a micro-rem photon survey meter measured 17 mRem h^{-1}. The simulated contribution of neutron-induced gammas was 2.75 mRem h^{-1}. The bremsstrahlung x-rays dose was the difference between the two, or 14.25 mRem h^{-1}. 120 keV electrons impinging on the Al plate at the ion source was modeled as the x-ray source. The simulation recorded a dose rate of 2.57×10^{-18} rem h^{-1} per electron/s. The electron current was calculated to be 5.543×10^{15} electrons/s, or 0.89 mA. MCNPX 3D matrix calculations were performed to show the x-ray flux around this irradiation system. Results are displayed in figure 7(a). The 40 keV x-rays can be easily attenuated with 3 mm of lead shielding around the ion source of the neutron generator. While these x-rays are relatively easy to shield, neutron-induced prompt gammas are more difficult to shield because of their higher energy (figure 7 (b)). Majority of the prompt gammas are 2.2 MeV hydrogen capture gammas, ($H(n, \gamma)D$), produced within the neutron shield.

A detailed description of the equivalent dose to the hand and the effective dose to whole body from 10 min irradiation was presented by Sowers *et al* (2015). The simulated hand dose from neutrons was calculated to be 32.28 mSv. Measurements by Fuji electronic pocket dosimeter (EPD) and film badge indicated that the neutron dose was 31.74 mSv. MC estimated that the irradiation dose from photon was 6.31 mSv, of which 4.88 mSv was from x-ray and 1.43 mSv was from gamma rays. The bremsstrahlung spectrum from the Al plate at the ion source was modeled as the photon source and an over-response of 10.68% in the TLDs at the irradiation site was measured. These readings ranged from 36 to 48 mSv h^{-1}. After incorporating the overresponse factor of 1.1068 and contribution ratios between x-ray and gamma into the calculation, the estimated photon dose was between 5.13 and 6.85 mSv. Experimental results agreed closely with the MC results.

The whole body effective dose was calculated conservatively to be 268 μSv.

4. Discussion and future work

A customized irradiation assembly including optimized moderator and reflectors was selected and constructed in this work. This system's detection limit derived from hand phantoms was 0.64 ppm after 10 min of irradiation, 10 min of decay, and 30 min of measurement. The detection limit can be further improved by a factor of $\sqrt{2}$ by adding another 100% HPGe detector and by a factor of 1.33 by increasing the measurement time from 30 min to 60 min. Our group has already ordered another 100% HPGe. Therefore, it is logical to predict that, in a near future, a detection limit of 0.34 ppm can be reached with two detectors and 60 min of measurement time.

Apart from ICRP's estimation of 1 μg Mn/g bone, Zaichick and his colleagues summarized the Mn concentration in human bone from 15 different studies (Zaichick 2013). It ranges from 0.13 to 9.7, with a median value of 3.5 μg Mn/g dry bone. Taking into account a ratio of 1.6 between dry bone and wet bone (Kim *et al* 2004), it gives a median value of 2.2 μg Mn/g bone, which is higher than the ICRP value of 1 μg Mn/g bone. Another way to compare results is by taking into account the Mn/Ca ratio since Ca is the major component of bone and its proportion in bone is relatively stable. Table 3 lists the literature values that presented both Mn and Ca information that we could find.

The Mn/Ca ratios range from 0.63 to 5 μg Mn/g Ca, with the ICRP value as the highest. The controversial findings of whether ICRP underestimated or overestimated the Mn concentration can be partly explained by the different methods used to quantify the concentrations and also by age, gender, and environmental differences. It can also have resulted from chemical loss during the bone washing and fat removing process, which could lead to miscalculation of the inorganic component of bone. To determine Mn concentration in a more accurate manner, a non-invasive way that maintains the integrity of the elemental information of the bone is desirable. Thus, the *in vivo* NAA system proves to be advantageous over other methods. As the only group that has done *in vivo* human NAA study so far, Pejovic-Milic *et al* from McMaster University found that ICRP overestimated the amount of bone Mn (Pejovic-Milic *et al* 2008a, Chettle and Waker 2009). With a detection limit of l.6 μg Mn/g Ca or 0.32 μg Mn/g bone, their system was not able to detect bone Mn from non-exposed populations. This shows that the actual Mn concentration in bone was smaller than 0.32 ppm (μg Mn/g bone).

The current detection limit of our portable neutron irradiation system is 0.34 ppm, which may still be difficult to detect the Mn signal in population that is exposed to low level of Mn. However, it will be valuable to apply the technique to moderately and highly exposed populations, especially an occupationally exposed population. In addition, work is ongoing to further improve the detection limit of the system by increasing the thermal neutron flux, which can be achieved with a new and better D–D neutron generator configuration and higher neutron flux.

An occupational study is being carried out in Zunyi, China to use bone Mn as a biomarker to study the association between Mn exposure and neurodegeneration. Bone Mn concentrations in Mn-exposed welders and matched controls are measured using the system described in this paper, and neuro-tests are performed for these people. Results from this occupational study will be reported in our next paper.

Acknowledgments

This work was supported by the National Institute for Occupational Safety and Health (NIOSH) grants 1R21OH010044 and 1R21OH010700; the Purdue University Nuclear Regulatory Commission (NRC) Faculty Development Grant NRC-HQ-11-G-38-0006; and Purdue Bilsland Fellowship.

References

Arnold M, McNeill F, Stronach I, Pejovic-Milic A, Chettle D, Waker A. An accelerator based system for *in vivo* neutron activation analysis measurements of manganese in human hand bones. Med. Phys. 2002; 29:2718–24. [PubMed: 12462740]

Aschner M, Guilarte TR, Schneider JS, Zheng W. Manganese: recent advances in understanding its transport and neurotoxicity. Toxicol. Appl. Pharmacol. 2007; 221:131–47. [PubMed: 17466353]

Bouaziz O, Allain S, Scott C, Cugy P, Barbier D. High manganese austenitic twinning induced plasticity steels: a review of the microstructure properties relationships. Curr. Opin. Solid State Mater. Sci. 2011; 15:141–68.

Bouchard MF, Sauve S, Barbeau B, Legrand M, Brodeur ME, Bouffard T, Limoges E, Bellinger DC, Mergler D. Intellectual impairment in school-age children exposed to manganese from drinking water. Environ. Health Perspect. 2011; 119:138–43. [PubMed: 20855239]

Bush VJ, Moyer TP, Batts KP, Parisi JE. Essential and toxic element concentrations in fresh and formalin-fixed human autopsy tissues. Clin. Chem. 1995; 41:284–94. [PubMed: 7874782]

Butcher DJ, Zybin A, Bolshov MA, Niemax K. Speciation of methylcyclopentadienyl manganese tricarbonyl by high-performance liquid chromatography-diode laser atomic absorption spectrometry. Anal. Chem. 1999; 71:5379–85. [PubMed: 21662735]

Chen, R., McKeever, SWS. Theory of Thermoluminescence and Related Phenomena. Singapore: World Scientific; 1997.

Chettle D, Waker A. Opportunities to improve the *in vivo* measurement of manganese in human hands. Phys. Med. Biol. 2009; 54:17. [PubMed: 19060358]

Crossgrove J, Zheng W. Manganese toxicity upon overexposure. NMR Biomed. 2004; 17:544–53. [PubMed: 15617053]

Huang CC, Chu NS, Lu CS, Wang JD, Tsai JL, Tzeng JL, Wolters EC, Calne DB. Chronic manganese intoxication. Arch. Neurol. 1989; 46:1104–6. [PubMed: 2803069]

Snyder, WS. I.C.o.R.P.T. Group. Report of the Task Group on Reference Man. Oxford: Pergamon; 1975.

Jiang YM, Mo XA, Du FQ, Fu X, Zhu XY, Gao HY, Xie JL, Liao FL, Pira E, Zheng W. Effective treatment of manganese-induced occupational Parkinsonism with p-aminosalicylic acid: a case of 17-year follow-up study. J. Occup. Environ. Med. 2006; 48:644–9. [PubMed: 16766929]

Kim W, Donalson L, Herrera P, Woodward C, Kubena L, Nisbet D, Ricke S. Research note: effects of different bone preparation methods (fresh, dry, and fat-free dry) on bone parameters and the correlations between bone breaking strength and the other bone parameters. Poultry Sci. 2004; 83:1663–6. [PubMed: 15510550]

Levy BS, Nassetta WJ. Neurologic effects of manganese in humans: a review. Int. J. Occup. Environ. Health. 2003; 9:153–63. [PubMed: 12848244]

Liu Y, Byrne P, Wang H, Koltick D, Zheng W, Nie LH. A compact DD neutron generator-based NAA system to quantify manganese (Mn) in bone *in vivo*. Physiol. Meas. 2014; 35:1899–911. [PubMed: 25154883]

Liu Y, Koltick D, Byrne P, Wang H, Zheng W, Nie LH. Development of a transportable neutron activation analysis system to quantify manganese in bone *in vivo*: feasibility and methodology. Physiol. Meas. 2013; 34:1593–609. [PubMed: 24165395]

Mostafaei F, McNeill F, Chettle D, Prestwich W. Improvements in an *in vivo* neutron activation analysis (NAA) method for the measurement of fluorine in human bone. Physiol. Meas. 2013a; 34:1329. [PubMed: 24045335]

Mostafaei F, McNeill F, Chettle D, Prestwich W, Inskip M. Design of a phantom equivalent to measure bone-fluorine in a human's hand via delayed neutron activation analysis. Physiol. Meas. 2013b; 34:503. [PubMed: 23587669]

O'Neal SL, Hong L, Fu S, Jiang W, Jones A, Nie LH, Zheng W. Manganese accumulation in bone following chronic exposure in rats: steady-state concentration and half-life in bone. Toxicol. Lett. 2014; 229:93–100. [PubMed: 24930841]

Pejovic-Milic A, Chettle DR, McNeill FE. Quantification of manganese in human hand bones: a feasibility study. Phys. Med. Biol. 2008a; 53:4081–92. [PubMed: 18782941]

Pejovic-Milic A, Chettle D, McNeill F, Pysklywec M, Oudyk J. A preliminary study for non-invasive quantification of manganese in human hand bones. Phys. Med. Biol. 2008b; 53:N371. [PubMed: 18765892]

Pejovic-Milic A, Chettle DR, Oudyk J, Pysklywec MW, Haines T. Bone manganese as a biomarker of manganese exposure: a feasibility study. Am. J. Ind. Med. 2009; 52:742–50. [PubMed: 19753565]

Rodier J. Manganese poisoning in Moroccan miners. Br. J. Ind. Med. 1955; 12:21–35. [PubMed: 14351643]

Snyder, W., Cook, M., Nasset, E., Karhausen, L., Howells, GP., Tipton, I. Report of the Task Group on Reference Man. Oxford: Pergamon; 1975.

Sowers D, Liu Y, Mostafaei F, Blake S, Nie LH. A dosimetry study of deuterium–deuterium neutron generator-based *in vivo* neutron activation analysis. Health Phys. 2015; 109:566–72. [PubMed: 26509624]

Valentin J. Basic anatomical and physiological data for use in radiological protection: reference values: ICRP publication 89. Ann. ICRP. 2002; 32:1–277.

Wang JD, Huang CC, Hwang YH, Chiang JR, Lin JM, Chen JS. Manganese induced parkinsonism: an outbreak due to an unrepaired ventilation control system in a ferromanganese smelter. Br. J. Ind. Med. 1989; 46:856–9. [PubMed: 2611159]

Wennberg A, Iregren A, Struwe G, Cizinsky G, Hagman M, Johansson L. Manganese exposure in steel smelters a health hazard to the nervous system. Scand. J. Work Environ. Health. 1991; 17:255–62. [PubMed: 1925437]

World Health Organization. Hydrogen Sulfide: Environmental Health Criteria 19. Geneva: WHO; 1981.

Yildirim EA, Essizoglu A, Koksal A, Dogu B, Baybas S, Gokalp P. Chronic manganese intoxication due to methcathinone (ephedron) abuse: a case report. Turk. J. Psychiatry. 2009; 20:294–8.

Zaichick V. Chemical elements of human bone tissue investigated by nuclear analytical and related methods. Biol. Trace Element Res. 2013; 153:84–99.

Zhen Z, Xie J. Development of manganese-based nanoparticles as contrast probes for magnetic resonance imaging. Theranostics. 2012; 2:45. [PubMed: 22272218]

Zhu H, Wang N, Zhang Y, Wu Q, Chen R, Gao J, Chang P, Liu Q, Fan T, Li J. Element contents in organs and tissues of Chinese adult men. Health Phys. 2010; 98:61–73. [PubMed: 19959952]

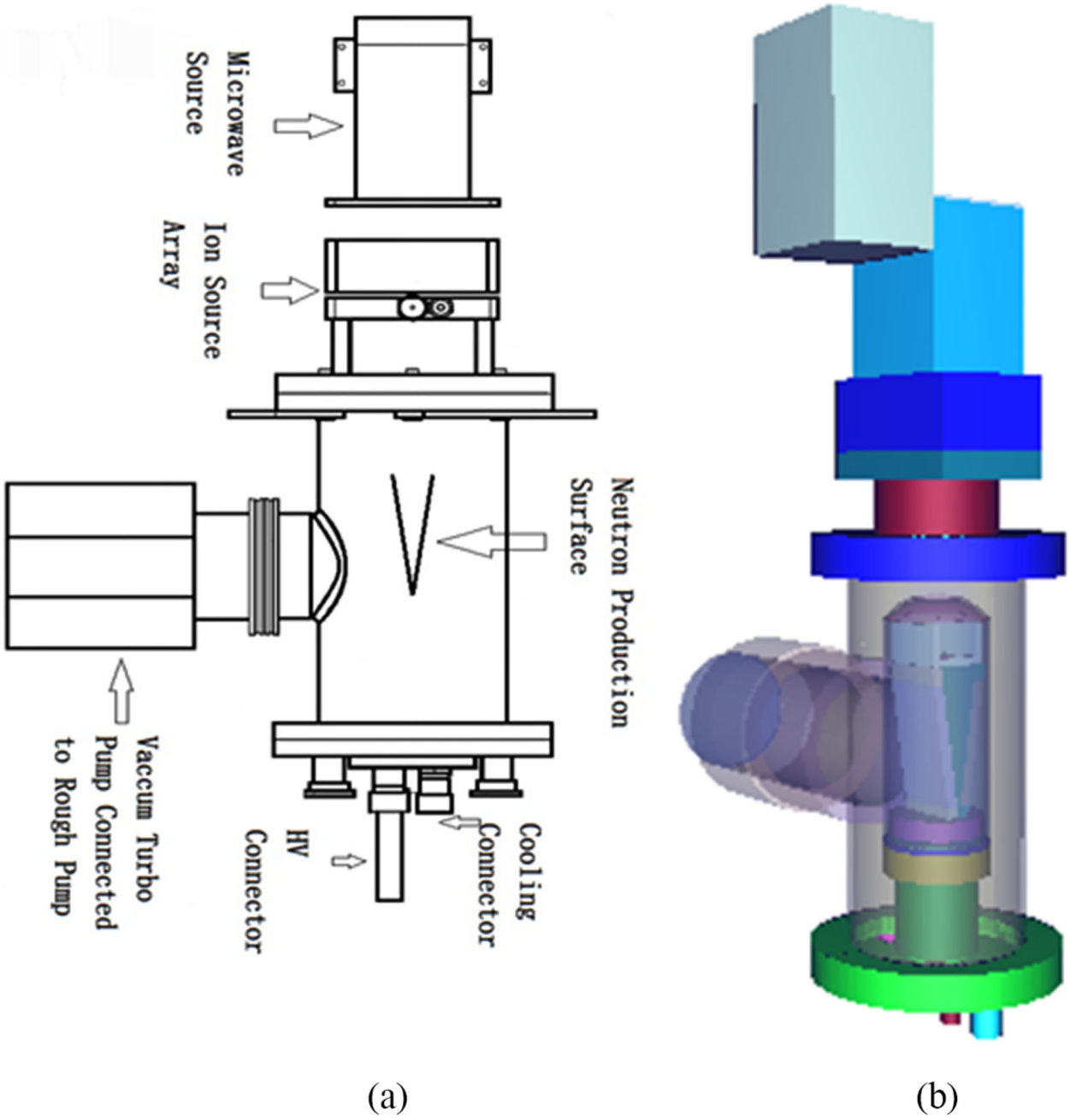

Figure 1.
A 2D diagram of the neutron generator head provided by the manufacturer (a) and its corresponding 3D model constructed in this work through MCNPX (b).

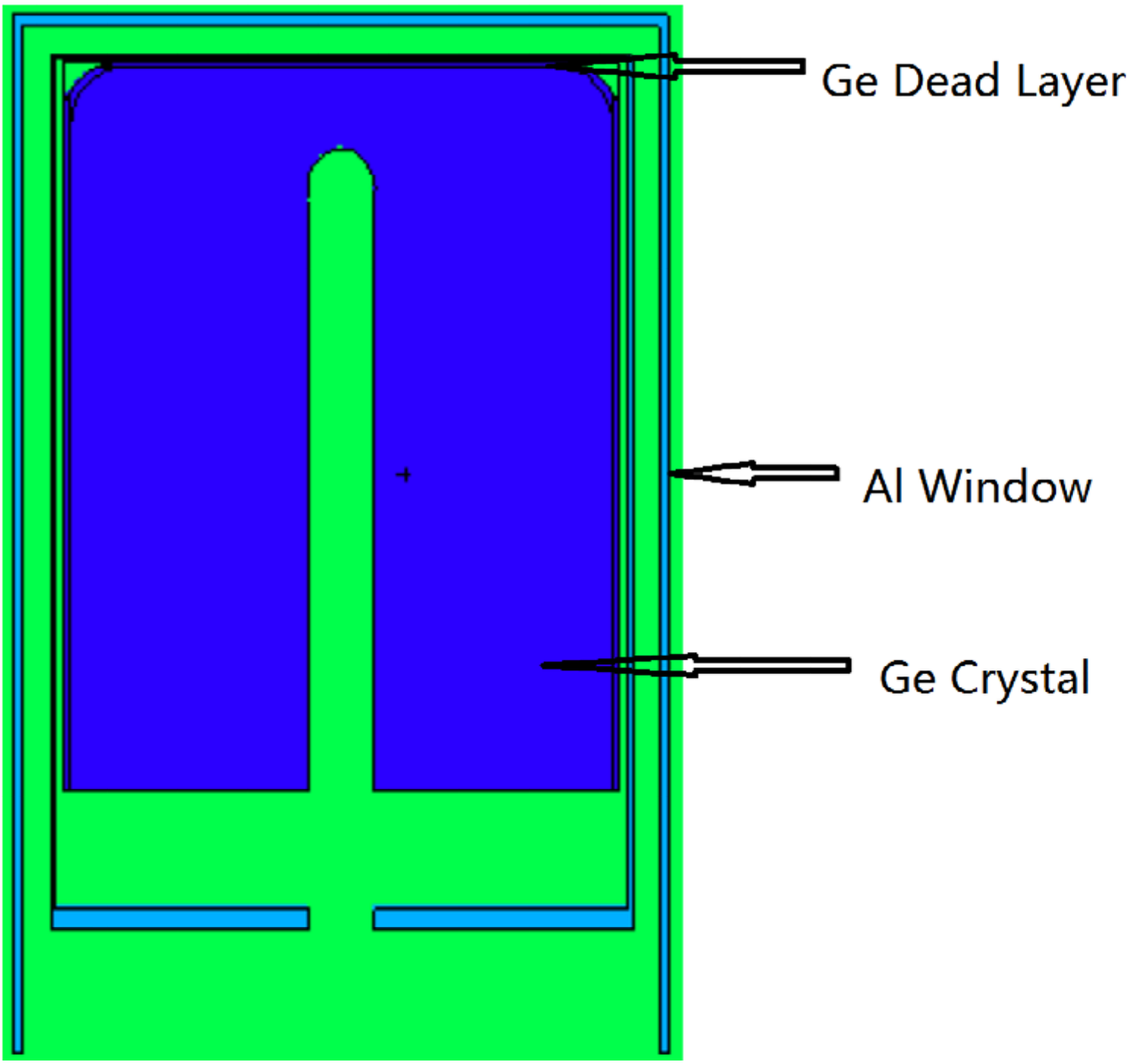

Figure 2.
Schematic diagram of MCNPX model for the p-type HPGe detector (model GMX90P4-ST).

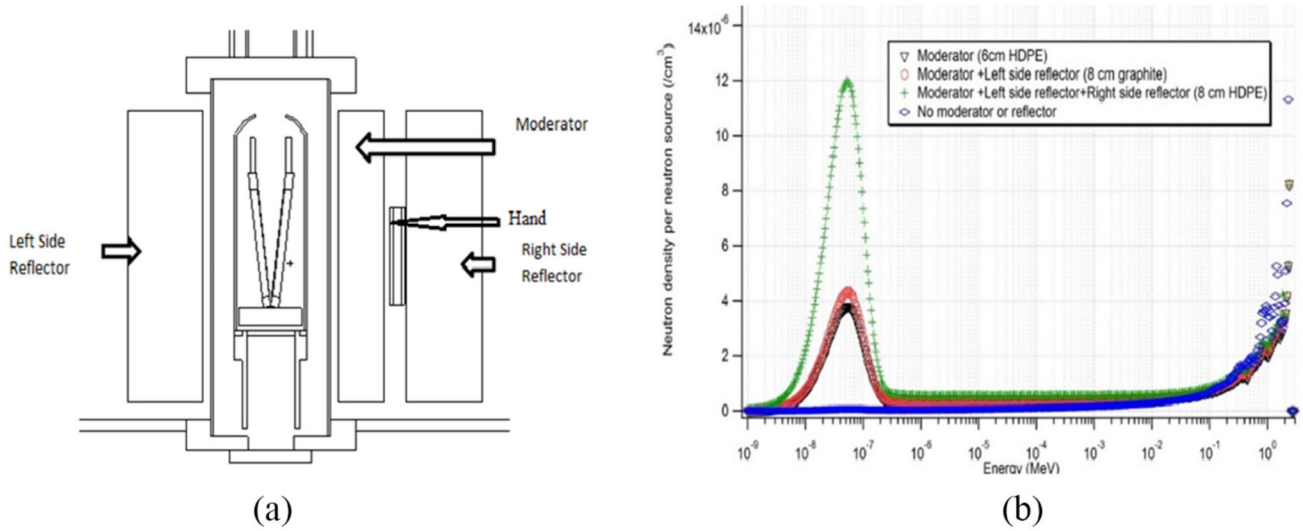

Figure 3.

MCNP simulation layout (a); summary of the thermal neutron enhancement by adding the optimized moderator and reflectors to the DD generator head (b).

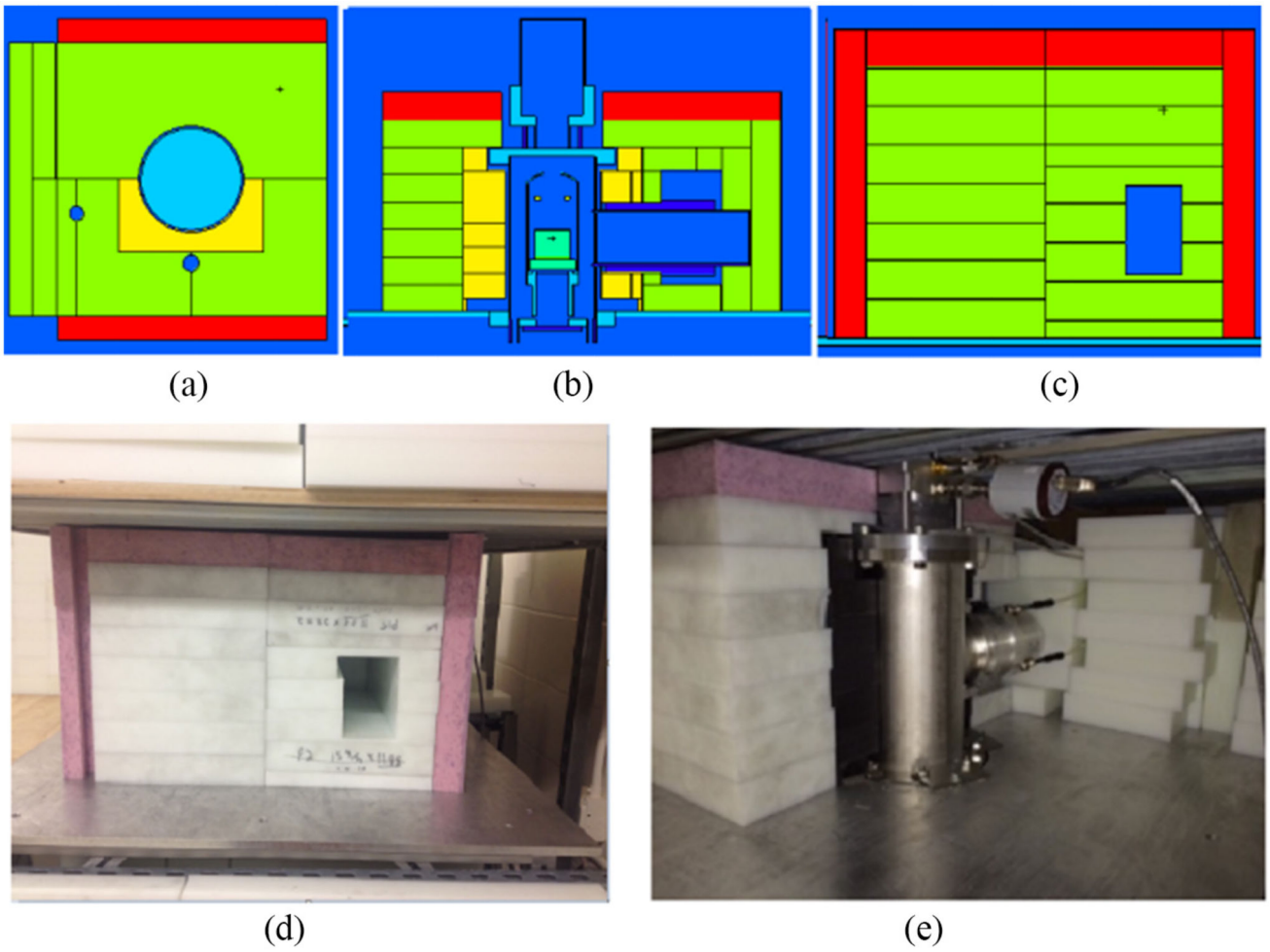

Figure 4.

Customized blocks inputted to MCNPX and the actual assembly. (a)–(c) MCNPX cross-section view on *XY*, *XZ*, *YZ* plane; (d)–(e) side view on *YZ*, *XZ*.

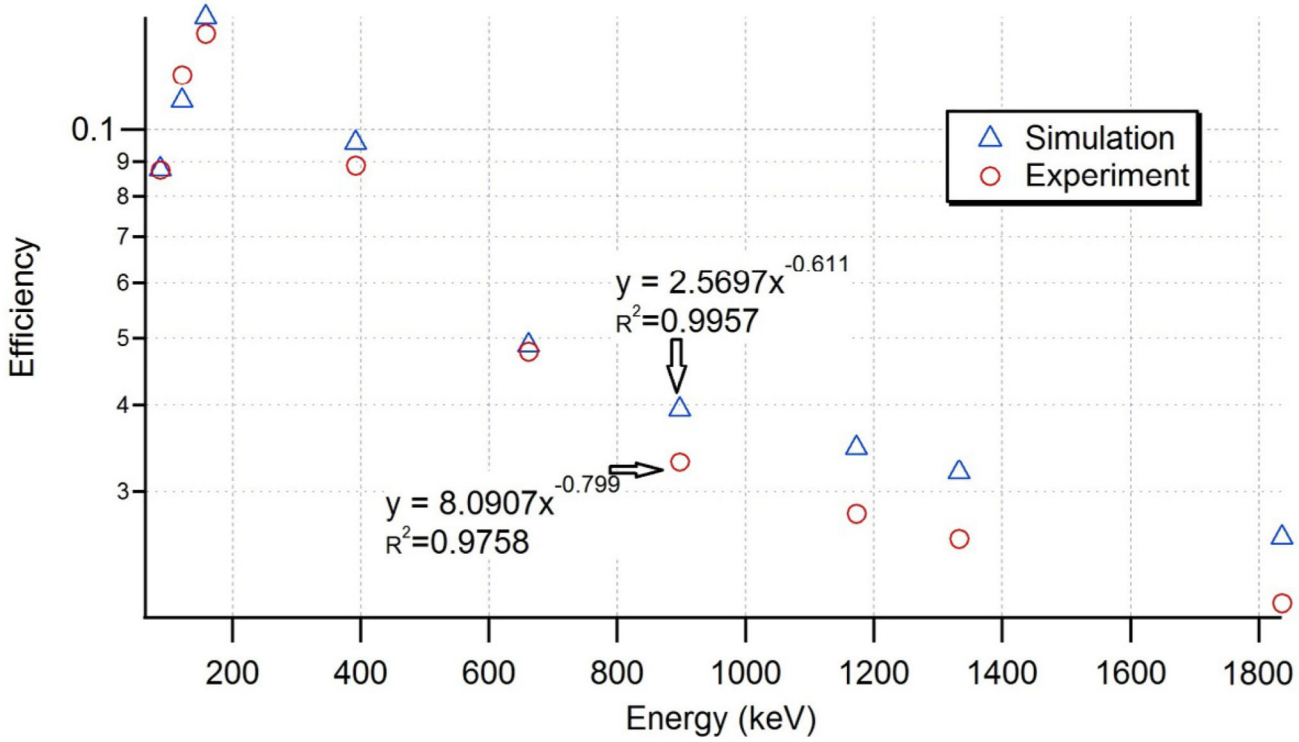

Figure 5.

Energy efficiency calibrations from simulation and experimental results. After adjusting the HPGe detector configuration in the MC model, radionuclides in the lower energy range (<898 keV) are in good accordance with experimental results. But due the summing effects, Y-88 and Co-60 efficiencies were experimentally underestimated.

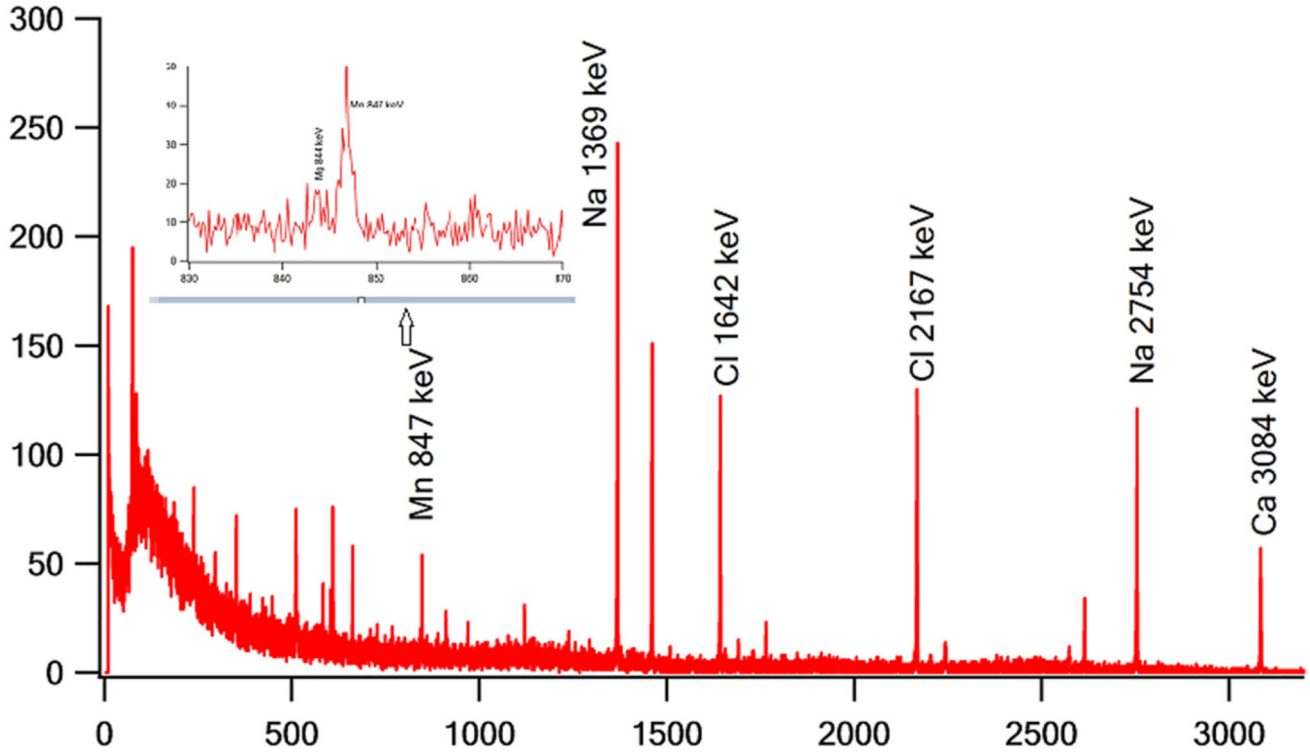

Figure 6.

Spectrum collected from 7.5 ppm hand phantom, irradiated for 10 min, decayed for 10 min and followed by a 30 min measurement.

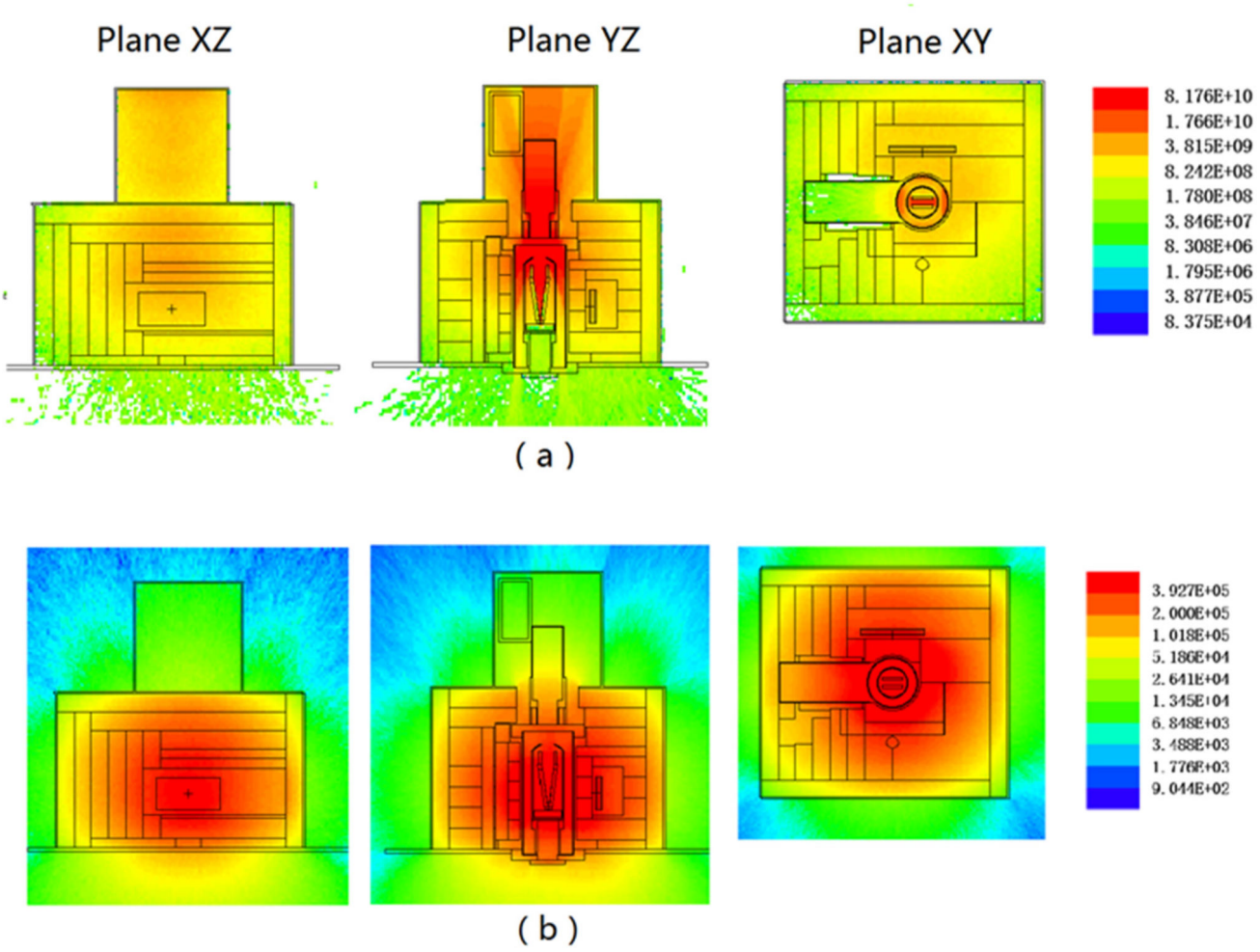

Figure 7.

MCNPX 3D matrix calculation plot of the photon flux from the D–D neutron generator surrounded by a customized moderator and reflector and 3 mm lead shielding. (a) X-rays produced by a current of 0.89 mA of electrons impacting the ion source plate, in units of x-rays/cm^2 per second; x-rays are fully shielded by 3 mm of lead except where cable and tubes are attached; here the x-ray leakage is negligible. (b) Neutron-induced prompt gammas produced in the HDPE blocks, in units of gamma rays/cm^2 per second when the flux of 2.45 MeV neutron source emission rate is 7×10^8 neutrons/s. These can't be attenuated by 3 mm lead.

Table 1

Efficiency comparison between experiment and simulation before and after adjustment of the HPGe dead layer thickness and distance of the Al window from crystal.

			Simulated efficiency		Difference between simu and exp (%)	
Radio-nuclide	**Energy (keV)**	**Experimental efficiency**	**Before adjustment**	**After adjustment**	**Before adjustment**	**After adjustment**
Am-241	60	0.051 ± 0.003	0.099	0.055	94.12	7.84
Cd-109	88	0.087 ± 0.004	0.131	0.092	50.57	5.75
Co-57	122	0.120 ± 0.006	0.163	0.128	35.83	6.67
Te-123m	159	0.137 ± 0.007	0.194	0.145	41.61	5.84
Sn-113	392	0.089 ± 0.004	0.117	0.096	31.46	7.87
Cs-137 (Multi-nuclide)	662	0.048 ± 0.002	0.059	0.049	22.92	2.08
Cs-137 (Point source)	662	0.088 ± 0.004	0.113	0.092	28.41	4.55

Author Manuscript

Author Manuscript

Author Manuscript

Table 2

Mn/Ca ratio comparison between experiment and simulation.

Phantom (ppm)	^{56}Mn	^{49}Ca	Experimental ratio	Simulated ratio
0	35.67 ± 5.04	400.26 ± 4.67	0.089 ± 0.013	0
7.5	214.67 ± 8.46	623.80 ± 5.11	0.344 ± 0.014	0.198
15	446.71 ± 10.18	656.94 ± 5.15	0.680 ± 0.016	0.397
22.5	517.56 ± 10.07	649.46 ± 4.96	0.800 ± 0.017	0.595
30	628.80 ± 8.41	652.16 ± 5.18	0.964 ± 0.015	0.794

Table 3

Literature values of Mn/Ca ratio.

	ICRP 23 (Snyder and I.C.o.R.P.T. Group 1975)	Zaichick (2013)	Zhu *et al* (2010)	Bush *et al* (1995)
Mn (μg/g bone)	1	0.273	0.448	0.14
Ca (g/g bone)	0.2	0.183	0.11	0.222
Mn/Ca ratio (μg/g)	5	1.5	4.07	0.63